



Available online at www.sciencedirect.com



Journal of Volcanology and Geothermal Research 150 (2006) 378–394

Journal of volcanology
and geothermal research

www.elsevier.com/locate/jvolgeores

Volcanic particle aggregation in explosive eruption columns. Part II: Numerical experiments

C. Textor^{a,*}, H.F. Graf^{a,1}, M. Herzog^{a,2}, J.M. Oberhuber^{b,3},
William I. Rose^c, G.G.J. Ernst^{c,d,4}

^a Max-Planck-Institut für Meteorologie, Hamburg, Germany

^b Deutsches Klimarechenzentrum GmbH, Hamburg, Germany

^c Department of Geological Engineering and Sciences, Michigan Technological University, Houghton, MI USA

^d Department of Earth Sciences, University of Bristol, UK

Received 16 September 2004; received in revised form 6 September 2005; accepted 16 September 2005

Available online 20 December 2005

Abstract

The goal of this paper is to determine the parameters that control the aggregation efficiency and the growth rate of volcanic particles within the eruption column. Numerical experiments are performed with the plume model ATHAM (Active Tracer High resolution Atmospheric Model). In this study we employ the parameterizations described in a companion paper (this issue). The presence of hydrometeors promotes the aggregation of ash particles, which strongly increases their fall velocities and thus their environmental impact. The tephra mass is about two orders of magnitude greater than that of hydrometeors during typical Plinian eruptions without interaction of external water. Ice is highly dominant in comparison to liquid water (>99% by mass). This is caused by the fast column rise (>100 m s⁻¹ on average) to very cold altitudes. Most particles occur in the form of frozen aggregates with low ice content.

The collection efficiency is governed by the availability of hydrometeors acting as adhesives at the particles' surface in our study, and wet ash particles have a higher sticking capacity than icy ones. Therefore, aggregation is fastest during the eruption within the column when limited regions of liquid water exist and when particle concentrations are very high (of the order of 10⁵ cm⁻³). Increased humidity in the background atmosphere generally leads to enhanced ice formation, but shows only a weak influence on the aggregation process. First sensitivity studies showed, however, a significant increase of the liquid water fraction when considering salinity effects. The availability of water or ice at the particles' surfaces is also governed by the surface properties, the porosity and permeability of ash, which are not well established to date. Particle growth is significantly enhanced for greater differences in the sizes and fall velocities among particles, as gravitational capture becomes more efficient. Our experiments indicate a major influence of the erupted particle size distribution. First sensitivity studies show that electrostatic forces result in a significant enhancement of aggregated particles.

The present exploratory study provides new insights into the sensitivity of the ash aggregation process to a number of key parameters. Our results indicate the need of further constraining particle composition, size, porosity, permeability, and surface

* Corresponding author. Present address: Laboratoire des Sciences du Climat et de l'Environnement, Gif-sur-Yvette, France.
E-mail address: christiane.textor@gmx.de (C. Textor).

¹ Present address: Department of Geography, University of Cambridge, UK.

² Present address: NOAA Geophysical Fluid Dynamics Laboratory (GFDL), Princeton, USA.

³ Now at a private company.

⁴ Present address: Mercator and Ortelius Research Centre for Eruption Dynamics, Department of Geology and Soil Science, University of Ghent, Belgium.

properties at low temperatures by in situ observations in the laboratory and in the field. In addition further research on electrostatic aggregation would be desirable.

© 2005 Elsevier B.V. All rights reserved.

Keywords: ash particle aggregation; cloud microphysics; numerical simulation; volcanic eruption column; hydrometeors; gas particle separation

1. Introduction

This paper continues our study on ash aggregation efficiency. In Paper I (Textor et al., 2005—this issue) we have discussed the importance of ash aggregation for the eruption column development. Information on the geometry, dynamics and thermodynamics, and on the properties and the fate of volcanic particles in the eruption column have been provided. Paper I focuses on the description of the parameterizations of ash aggregation in the plume model ATHAM (Oberhuber et al., 1998; Graf et al., 1999; Herzog et al., 2003; Textor et al., 2003a). The objective of this second part of our study (Paper II) is to determine the parameters that control the aggregation efficiency and the growth rate of volcanic particles within the eruption column through numerical experiments with the ATHAM model. We apply the parameterizations described in Paper I, and present a number of sensitivity studies where we test the influence of individual parameters on ash aggregation efficiency.

After a short introduction of the ATHAM model and its setup for this study in Sections 2 and 3, we describe the results from the numerical simulations. In Section 4.1 we explain the reference experiment REF, and present the general characteristics of tephra, hydrometeors, and the particle properties in the eruption cloud. We show the importance of considering ash aggregation processes when we compare the results of a simulation without aggregation to the REF simulation in Section 4.2. The importance of salinity effects is discussed in Section 4.3. The effect of particle morphology is investigated in Section 4.4 where we modify the collection efficiency. The impact of electrostatic forces and that of the initial particle size distribution are examined in Sections 4.5 and 4.6, respectively. Finally, in Section 4.7, we present simulations for different atmospheric background conditions.

For definitions of the indices, variables and terms used throughout this study see Table 1 in Paper I.

2. Plume model ATHAM

We perform numerical experiments with the non-hydrostatic, non-steady plume model ATHAM, which is designed to simulate the dispersal of an eruption

column resulting from an explosive volcanic event. The numerical experiments begin just after the earliest mixing of the erupting gas-particle-mixture with ambient air, when the flow adjustment to atmospheric pressure has already taken place, see Section 3 of Paper I. The high-pressure regime in the conduit and at the vent, the shock-like expansion of the erupting mixture, and the small scale processes including potential particle aggregation in the vicinity of the crater are not resolved in the concept of ATHAM. We focus on processes in the eruption column during eruption and shortly afterwards, in the range of some tens of meters to some tens of kilometers. The simulation time is some hours, covering spatial scales of some hundreds of kilometers. ATHAM predicts the temporal and spatial eruption column development; the only prescribed quantities are the parameters of the volcanic eruption and the conditions in the ambient atmosphere. The input of volcanic material during the eruption is specified by the vertical velocity, temperature and composition of the ejecta at several grid points representing the base of the pressure-adjusted eruption column. The full set of Navier–Stokes equations is solved for volume mean quantities using a finite difference method with an implicit time step scheme on a regular grid. The model formulations do not vary with the distance from the vent: the same set of equations for the dynamics, thermodynamics and microphysics is calculated at each grid point at every time step. ATHAM has been successfully used to simulate the evolution of a volcanic cloud in the atmosphere (Oberhuber et al., 1998; Herzog et al., 1998, 2003; Graf et al., 1999; Textor et al., 2003a,b). In addition, it has been used for the simulation of biomass burning events (Trentmann et al., 2002, 2003). In this study the following processes are accounted for:

The dynamics module solves the Navier–Stokes equations for the gas-particle-mixture and treats the transport of active tracers including particle sedimentation. (Oberhuber et al., 1998; Herzog et al., 1998).

The turbulence closure scheme delivers the turbulent exchange coefficients for each dynamic quantity, thereby also describing the entrainment of ambient air into the eruption column (Herzog et al., 1998, 2003; Oberhuber et al., 1998).

The cloud microphysics module describes condensation of water vapor and formation of precipitation. All phases of water are included: vapor, liquid and solid. The feedback of the thermal energy changes on the dynamics is accounted for. A simplified parameterization allows for the consideration of the salinity effects from dissolved gases on the thermodynamical properties of hydrometeors in sensitivity studies (Textor et al., 2003a).

The ash microphysics module describes particle growth and coagulation based on microphysical interactions between hydrometeors and ash (Paper I). A simplified parameterization of the influence of electrostatic forces on ash aggregation is included for sensitivity studies.

The gas scavenging module describes the scavenging of volcanic gases by liquid and frozen particles, and the chemical dissociation of the solutes in water (Textor et al., 2003a,b).

3. Model setup

We do not try to simulate a specific eruption, but choose conditions typical for highly explosive events. In addition, we focus on the fate of the fine particle fraction: Firstly, because it dominates the particle mass in the atmosphere (Sparks et al., 1997); secondly, because only fine ash is relevant in the assessment of mesoscale effects from an eruption; thirdly it dominates the injection of solid material into the stratosphere. The axis-symmetric version of ATHAM is employed here, for the sake of saving computer memory and time. The dilution of the mixture by entrainment of surrounding air corresponds to a three dimensional simulation with an atmosphere initially at rest (Herzog et al., 2003). The effects of a mean lateral wind are not considered; the flow pattern in the atmosphere is only influenced by the eruption column. The results from our experiments are suitable to investigate the fundamental features of a volcanic eruption column.

The experiments are performed on a stretched grid with 150×80 points. The model domain is 300 km in the horizontal and 50 km in the vertical direction. In the center of the model domain, where the volcano is situated, we use a spatial resolution of 250 m in the horizontal and 300 m in the vertical, at the lateral boundaries the horizontal resolution is about 5 km. This grid choice allows for the eruption column dispersal without disturbances from the model boundaries over our simulation time of 90 min. We choose typical volcanic conditions at the eruption column base for a

Plinian eruption. The initial conditions at the base of the eruption column summarized hereafter are the same for all experiments performed in this study.

Plume base height 750 m above sea level;
Eruption column base radius $r_{\text{ad}} = 375$ m;
Vertical velocity $w_b = 400$ m s $^{-1}$;
Temperature $T = 1100$ K;
Gas mass fraction $q_e = 7.34$ wt.%;
Water vapor fraction of gas about $q_v = 82$ wt.%;
Particle mass fraction $q_{\text{ax}} = 92.66$ wt.%;
Ash particle density $\rho_{\text{ax}} = 1800$ kg m $^{-3}$;
Density of the gas-particle-mixture $\rho_{\text{mix}} \sim 2.6$ kg m $^{-3}$;
Mass eruption rate $\dot{M} \sim 4.5 \cdot 10^8$ kg s $^{-1}$.

The density of volcanic juvenile particles is highly variable (see also Section 3 in Paper I), in our experiments we choose for illustration purposes an intermediate value. The temperature of the erupted mixture does not significantly change during expansion until pressure-adjustment, because of the high concentration of particles which have a large heat capacity. Thus, we can use temperature data obtained from thermo-chemical calculations to initialize the model (for references see Sparks et al. (1997)). We neglect the topography of the volcanic crater and use a flat surface, because the ATHAM simulations start after adjustment to ambient pressure some hundreds of meters above the crater. The vertical velocity at the eruption column base w_b is set to twice the speed of sound of the mixture c_s , see Section 3 in Paper I:

$$w_b = 2c_s = 2\sqrt{\frac{c_{p,e}}{c_{v,e}}(c_{p,e} - c_{v,e})T q_e} \quad (1)$$

c_p and c_v are the specific heat capacities of the gases at constant pressure and volume, respectively. q is the mass mixing ratio and T the temperature. The index e refers to the gas phase. Using the specific heat capacities for air and water vapor, we get for the speed of sound of the mixture $c_s = 210$ m s $^{-1}$, and set for the initial vertical velocity we $w_b = 400$ m s $^{-1}$. Within the first 60 s, the eruption velocity is increased to its maximum value. It is kept constant for the following 27 min and then reduced to zero during the last 3 min of the eruption. We continue the experiment for an additional 60 min in order to investigate the post-eruptive development of the eruption cloud.

The density of the gas-particle mixture ρ_{mix} is obtained from the volume ratio of particles and gas:

$$\rho_{\text{mix}} = \frac{q_e + q_{\text{ax}}}{q_e/\rho_e + q_{\text{ax}}/\rho_{\text{ax}}} \quad (2)$$

with q indicating the mass mixing ratios and the indices a and e referring to ash and gas, respectively. The gas density is taken from the ideal gas law.

We choose a mass eruption rate \dot{M} typical for a highly explosive event (e.g., Sparks et al., 1997). The radius at the base, rad , of the pressure-adjusted eruption column is then calculated from rearranging the following equation:

$$\dot{M} = 2\pi rad \rho_{mix} w_b. \quad (3)$$

With $\dot{M} \approx 4.5 \cdot 10^8 \text{ kg s}^{-1}$ and $w_b = 400 \text{ m s}^{-1}$ we get an eruption column base radius of $rad = 375 \text{ m}$.

The particle size distribution (see also Section 3 in Paper I) for the REF experiment has been chosen similar to that of the eruption of Mt. St. Helens (1980) (MSH). The estimated total ash size distributions are illustrated in Fig. 1. The thin solid line shows the log-normal distribution given in Woods and Bursik (1991) (WB). The thick solid line presents the particle size data of Carey and Sigurdsson (1982) (CS), which were obtained by directly sampling the deposited ash. The CS data are shown as mass per size interval versus constant size intervals ($\Delta r = 1 \mu\text{m}$). This is different from the original presentation where non-constant phi-classes were used as size intervals, see CS for details. The bimodal structure of the particle distribution, which was also observed at other volcanoes (for references see Sparks et al., 1997), is much less pronounced in our presentation where phi-class-intervals

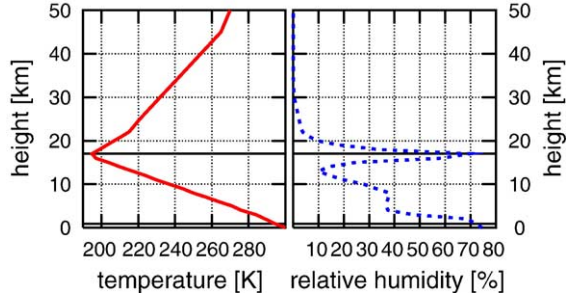


Fig. 2. Atmospheric profiles for temperature and relative humidity in the REF experiment taken from McClatchey et al., 1972. The ground level at 750 m and the tropopause at 17 km are indicated by horizontal lines.

were used. The CS data neither include the smallest particles which were transported further away, nor the largest which fell within 50 km of the crater. This explains the absence of smaller particles in the CS data when compared to those of WB.

We employ two particle modes, which are described by gamma functions as explained in Section 4.2 in Paper I, to represent the CS data. The radii of average mass of the two particle modes are $\bar{r}_{ac} = 2.5 \mu\text{m}$ and $\bar{r}_{ap} = 50 \mu\text{m}$, respectively, with the latter contributing 60% to the total erupted ash mass. These functions are also shown in Fig. 1. The skewness parameters of the gamma distributions are both set to $v = 1$. Our size distribution is characterized by a more pronounced bimodality than the CS data, in order to investigate the effect of contrasting particle sizes within the simplified modal approach used in ATHAM, see Section 4 in Paper I. Furthermore, the bimodality could be attributed to early electrostatic aggregation within and close to the vent, which is not captured in our simulation. In a sensitivity study discussed in Section 4.6, we approximate data of the particle distribution of Askja D as an example for a Plinian eruption in order to examine the effect of the initial particles size distribution on ash aggregation.

The fate of volcanic gases (SO_2 , HCl , HBr , and H_2S) in the eruption column was examined in a previous paper (Textor et al., 2003a). The effect of dissolved volcanic species on the thermodynamic properties of water and ice (salinity effects), are represented by the concentration of dissolved volcanic gases.

In the reference experiment the ambient conditions for pressure, temperature and humidity correspond to standard atmospheric profiles for the subtropics taken from McClatchey et al. (1972), with the tropopause at about 17 km as shown in Fig. 2. The ambient conditions are modified in the sensitivity studies discussed in Section 4.7.

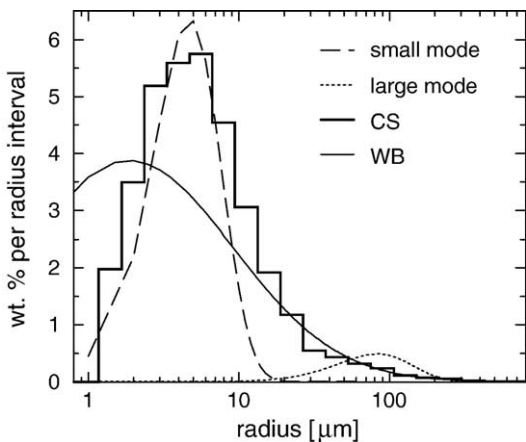


Fig. 1. Particle size distribution of the MSH ash. The data of CS (thick solid line) and log-normal distribution given by WB (thin solid line) are shown. The two gamma distributions (dashed and dotted lines) represent the particle size distributions of the two modes of erupted ash in ATHAM.

Table 1

List of numerical experiments performed within the study

Name	Modification with respect to the experiment REF
REF	Reference experiment
SALT	Consideration of salinity effects (Textor et al., 2003a)
NICE	Ice nucleation only at $T < -15^{\circ}\text{C}$
NBAC	Nucleation only on ash
AULA	Autoconversion in large cold category neglected
DRY	No ash aggregation
POR1	Collection efficiency of aggregates f_{POR1}
POR2	Collection efficiency of aggregates f_{POR2}
LIN1	Collection efficiency of aggregates f_{LIN1}
LIN2	Collection efficiency of aggregates f_{LIN2}
EICE	Collection efficiency of frozen particles E_{ICE}
ELS1	Collection efficiency of dry ash f_{ELS1}
ELS2	Collection efficiency of dry ash f_{ELS2}
ELS3	Collection efficiency of dry ash f_{ELS3}
ELS4	Collection efficiency of dry ash f_{ELS4}
ELS5	Collection efficiency of dry ash f_{ELS5}
ASK	Initial particle size distribution modified
SAS	Background atmosphere: sub arctic summer
SAW	Background atmosphere: sub arctic winter
MLS	Background atmosphere: midlatitude summer
MLW	Background atmosphere: midlatitude winter
STH	Background atmosphere: subtropical hot
STW	Background atmosphere: subtropical wet
TRO	Background atmosphere: tropical

A set of numerical experiments has been performed in this study. An overview of all experiments is given in Table 1.

4. Results

4.1. General characteristics of the eruption column in the reference experiment

In the REF experiment, the eruption column first penetrates the tropopause at 17 km about 5 min after the eruption starts. The average vertical velocity in the core of the column is greater than 100 m s^{-1} . The distribution of particles (hydrometeors, ash and aggregates) in the eruption column 30 min after the eruption onset is shown in Fig. 3.

The eruption column flow starts to diverge at about 15 km. The height of neutral buoyancy (HNB) is at about 23 km, 6 km above the tropopause. Above the central rising zone, overshooting by about 10 km occurs. The diameter of the umbrella cloud is about 150 km. The ash mass mixing ratio is several hundreds of g kg^{-1} in the central column and about 100 g kg^{-1} in the umbrella region. The particle concentrations within the eruption column are of the order of 10^5 cm^{-3} and 10^1 cm^{-3} for small and large particles, respectively. The mass of hydrometeors accounts only for a few percent

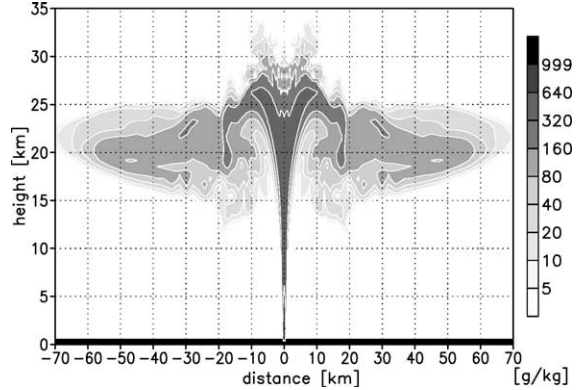


Fig. 3. Eruption cloud (x-z distribution) of particles (hydrometeors, ash, and aggregates) shown for the REF experiment after 30 min. The scale gives mass mixing ratio in g kg^{-1} tot.mass.

of the total particle mass in the eruption column after 30 min. Hence, aggregates are rather dry with hydrometeor fractions typically smaller than 10% by mass, see Fig. 4. Relatively ice-rich aggregates consisting of up to 25% ice by mass are formed by water vapor deposition on small particles at the HNB.

Fig. 5 depicts the vertical distribution, i.e., the horizontal integral of particles at each height level, at different times during the course of the simulation. The lower broad peak in the profiles indicates larger particles. These are aggregates that move downwards with time from the HNB at ≈ 23 km to about 5 km after 90 min (i.e., one hour after the eruption end) forming a deep fallout zone.

The large particles initially contribute 60 wt.% of the ash erupted at the vent in this experiment. Aggregation transfers an additional 30% of the small ash to the larger size classes, see also Figs 13, 16, and 22. The overall aggregation rate is highest at the beginning of the eruption, when all particles occur within the rising

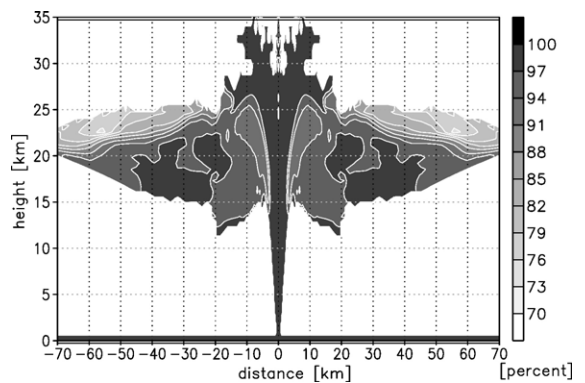


Fig. 4. Fraction of ash (x-z distribution) in hydrometeor-ash aggregates shown for the REF experiment after 30 min. The scale give the percentage of ash in relation to the total aggregate mass.

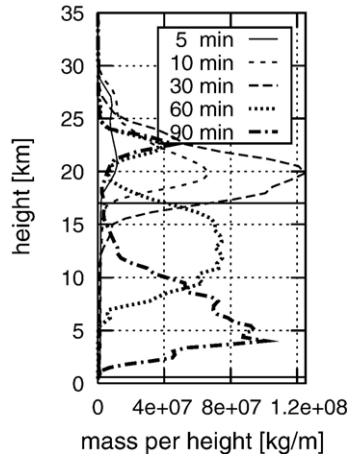


Fig. 5. Vertical distributions of particles in the REF experiment at 5, 10, 30, 60, and 90 min. Shown is the horizontal integral per height level in $\text{[kg m}^{-1}\text{]}$ of the sum of the masses of hydrometeors, ash, and aggregates. The plume base level at 750 m and the tropopause at 17 km are indicated by horizontal lines.

eruption column, where the particle concentration is extremely high and where some liquid water exists, see below. When the particles reach the HNB after about 5 min, the aggregation rate decreases, because the particle concentration decreases by about one order of magnitude. In addition, the collection efficiency decreases with decreasing temperatures. The aggregation rate increases for a short time after the eruption end, due to transient formation of liquid water in the central region of high particle density during gravitational fall-back over the vent region. After 40 min, aggregation is not very efficient any more, because of increasing dilution in the eruption cloud and decreasing availability of liquid water. The radii of average mass in the large particle classes are displayed in Fig. 6 a–c at 30, 60 and 90 min, respectively. We show either the liquid or the frozen class, whichever has the higher mass mixing ratio. The displayed radii refer to particles consisting of pure hydrometeor, pure volcanic ash or mixed hydrometeor–ash aggregates. Please note, that it is not possible for pure hydrometeors and ash particles to coexist in the same place in our model formulation (see Section 4 in Paper I).

Particle growth continues during lateral transport in the umbrella cloud. Thus, the biggest particles with mean volume radii larger than 100 μm can be found at the edges of the eruption column. The mean particles' terminal fall velocities increase with height from 3 to 7 m s^{-1} due to the decrease of friction at greater altitudes. With an average fall velocity of 4 m s^{-1} these particles need about 90 min to fall from the umbrella cloud to the ground.

The narrower stationary peak in Fig. 5 at HNB stems from small particles (about 2.5 μm in radius), that are suspended within the umbrella region. After 90 min, this cloud has a horizontal extent of more than 250 km, and contains 13% by mass of the erupted ash. The possibility of gravitational separation between the coarse ash fraction on the one hand and the finest ash, and gases, on the other hand, was suggested by, e.g., Lane and Gilbert (1992), Miura et al. (1996), and Holasek et al. (1996). Many examples of this phenom-

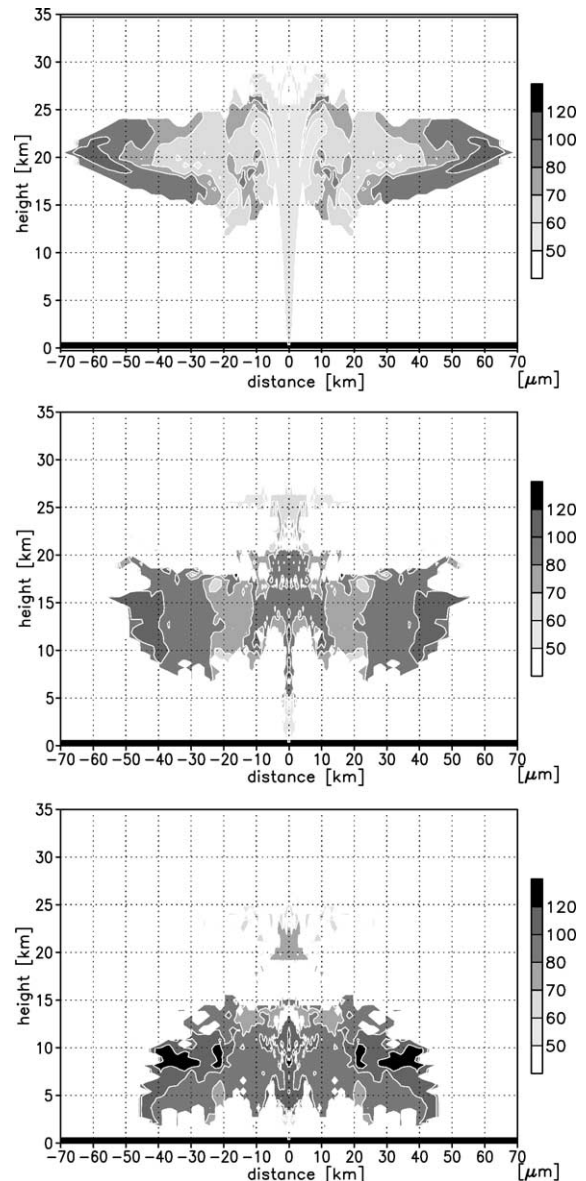


Fig. 6. Mean volume radii in the large particle mode (x-z distribution) at locations with mass mixing ratios $>5 \text{ g kg}^{-1}$. Shown at 30, 60, and 90 min for the REF experiment. The threshold in mass mixing ration leads to the irregular pattern in these figures.

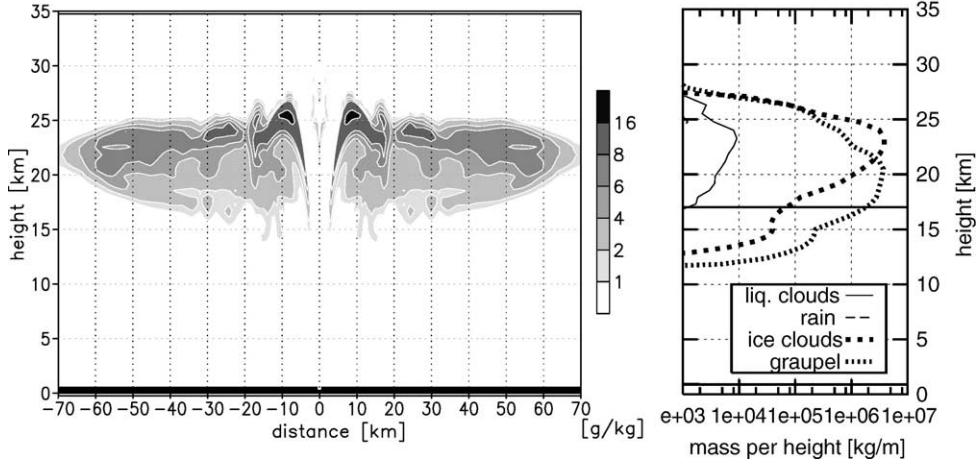


Fig. 7. Eruption cloud (x - z distributions) of all hydrometeors (mass mixing ratio in g kg^{-1}) (left panel). Related vertical distributions of each hydrometeor class (horizontal integral in mass per height level in kg m^{-1}). The plume base level at 750 m and the tropopause at 17 km are indicated by horizontal lines (right panel). Shown for the REF experiment after 30 min.

emon observed on satellite imagery have now been reported. For the 1982 El Chichón eruptions, Schneider et al. (1999) documented a spectacular case.

The cloud condensation level in the rising eruption column is at elevated altitudes in the tropopause region. The clouds of total condensed hydrometeors (liquid water plus ice) after 30 and 90 min, as well as the related vertical distributions for each hydrometeor class are plotted in Figs. 7 and 8, respectively.

Liquid phase microphysics is negligible in our simulation; the greatest fraction of the hydrometeors in the eruption cloud is taking the form of ice (>99% by mass after 30 min). This simulated prevalence of ice is supported by observations as discussed in Paper I. See however also our sensitivity experiments on the salinity effects in Section 4.3. The fast column rise

causes temperatures too low for even supercooled water to exist. The temperature field at 30 min of eruption is shown in Fig. 9.

Extreme horizontal temperature gradients occur both in the horizontal across the eruption column (from several hundreds of degrees Celsius in the center to ambient temperatures at the column edge) and in the vertical. At about 15 km height the core temperatures become lower than 100 °C. Some water, encircled by a hydrometeor-free region, occurs in the center of the eruption column above the flow divergence zone, see Fig. 7. This region is, however, decoupled from the rising column, the dynamical conditions are non-steady, and the stream pattern highly turbulent. The condensed water existing in this region stems from an earlier phase of the eruption before divergent flow of

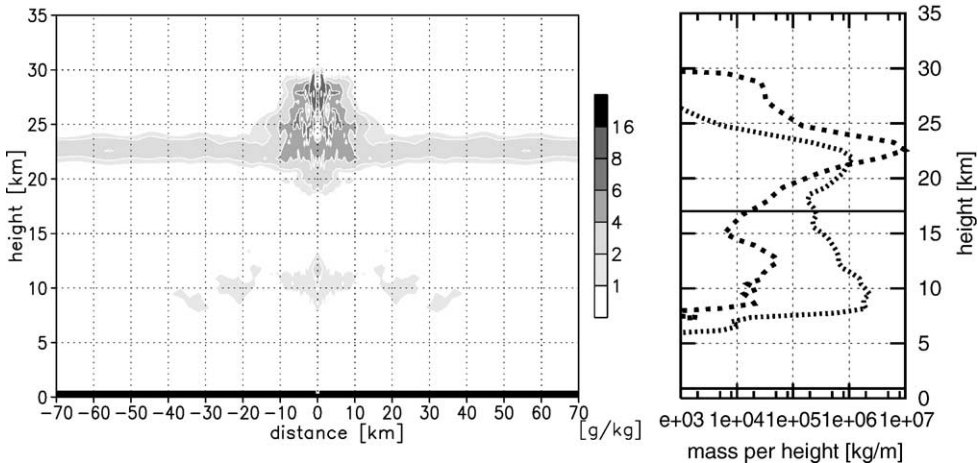


Fig. 8. Same as Fig. 7, but after 90 min (60 min after the end of the eruption). The horizontal extent of the hydrometeor cloud in the stratosphere is about 250 km.

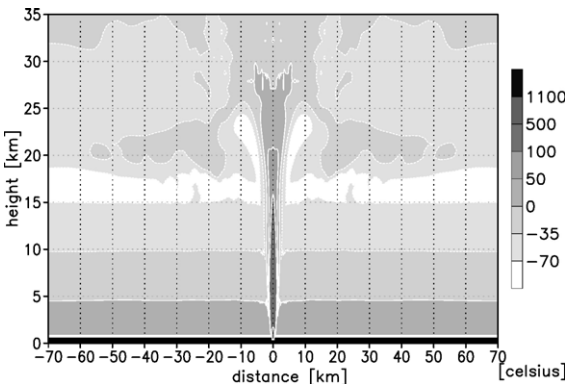


Fig. 9. Temperature in the eruption cloud (x - z distribution), shown for the REF experiment after 30 min. The scale gives temperature in $^{\circ}\text{C}$.

the column occurred. Rising water vapor condenses at the fringes of the rising eruption column at about 17 km height. Liquid water persists up to about 25 km within a narrow horizontal band of a few kilometers far enough from the hot core of the column, but where the temperature is still above freezing. The vertical velocity in this region is higher than 150 m s^{-1} . Thus, particles are in contact with water for a period shorter than one minute. At the beginning of the eruption, more than 95% of the ice is in the small particle class. Water vapor deposition in the rising eruption column occurs primarily on small particles, which provide most of the ash surface. Small particles grow by aggregation, thus transferring the ice with them to the larger particle class. From 10 min of eruption onwards, the larger class of settling ice-ash aggregates contains about half of the ice in the eruption column. The low relative humidity in the lower troposphere in our scenario (see Fig. 2), causes sublimation of ice above the melting level ($\approx 5 \text{ km}$). Below an altitude of approximately 8 km, liquid water and ice are almost entirely evaporated, see Fig. 8, and almost no rain reaches the ground (even when considering salinity effects, see Section 4.3). Thus, in the deposit of an eruption under the conditions investigated here, no hydrometeors would be detected, although they play a significant role during the evolution in the eruption column.

We tested the influence of decreased ice nucleation capacity in a sensitivity experiment tagged NICE, where we allowed the sublimation of water only for temperatures lower than -15.0°C . See also the discussion in Section 3 of Paper I on ice nucleation capacity of volcanic ash. The simulation results are unaffected because of the fast reduction of temperatures well below -15.0°C in the rising eruption column, see Fig. 9. We conclude that the microphysics is not very sensitive to changes in ice nucleation capacity with tem-

perature. Another sensitivity study called NBAC neglecting nucleation of frozen and liquid hydrometeors on non-volcanic particles in the background atmosphere (see Section 4.5 in Paper I) also produced little change our findings. We also examined the effect of neglecting intra-modal aggregation (autoconversion) of large cold particles (see Section 4.6.2 in Paper I) in a sensitivity study AULA. The amount of ash in the stratosphere is not changed when compared to the experiment REF, but the altitude of the tropospheric fallout zone is about 3 km higher, because the aggregates are smaller. Our experiment did not show a significant effect of intra-modal aggregation of large cold particles on the eruption column development during the first hour after eruption, however, more detailed experimental information on the aggregation of frozen icy ash is needed to validate this finding.

Observations of the ash deposits show millimeter-sized volcanic aggregates as reported in, e.g., Sparks et al. (1997). In our experiments, aggregates do not reach this size. In the following sections we investigate, under which conditions particle growth is more pronounced, and what factors control the aggregation efficiency.

4.2. Neglecting ash particle aggregation

The relevance of ash particle aggregation is investigated in this section. We compare the REF study with an experiment tagged DRY, in which we completely neglect interactions between ash particles and hydrometeors. Here, water vapor deposition on ash, and aggregation of coated particles is not considered. Ash is transported in the model, but does not take part in any microphysical process. The parameterizations presented in Paper I are applied only to pure hydrometeors. Fig. 10 depicts the vertical ash distributions at different times during the simulation. See also Fig. 5 for comparison with the REF experiment (note that the x -range is twice as large in DRY).

The evolution of two ash layers caused by the separation of the fine ash fraction, suspended at HNB, from the settling coarse particles is also visible, but sedimentation of the latter is much slower. At 90 min simulation time, the lower boundary of the settling layer, consisting of $50 \mu\text{m}$ particles, reaches a height of $\approx 10 \text{ km}$, whereas the larger aggregates in the experiment REF already reach the ground. In the DRY experiment, a larger mass fraction of erupted ash of about 40% remains above the tropopause, in contrast to about 13% in the REF study. Fig. 11 shows the mass fractions of erupted ash above a certain height at 90 min simulation time. Our experiments

show that the consideration of aggregation significantly influences the deposition behavior of volcanic ash, and its injection and residence time in the stratosphere.

4.3. Salinity effects

We examined the influence of salinity effects on the amount of condensed water and ice through numerical experiments tagged SALT. In a volcanic eruption column, hydrometeors contain dissolved gases and salts of unknown qualities and quantities, see for example Mackinnon et al. (1984), or Smith et al. (1982). Given the major uncertainties of the hydrometeor composition and the concentrations of multicomponent solutions it is not reasonable to apply a comprehensive thermodynamic model to simulate salinity effects. We therefore employ a highly simplified parameterization in order to assess a potential importance of this process. We approximate the salt concentration by that of dissolved volcanic gases, which ranges from 1 to 10 mol per kg H₂O in the experiment in REF. We employ simple functions reflecting non-ideal effects that enhance salinity effects on hydrometeors' thermodynamic properties. For a description of the parameterization of the salinity, see Textor et al. (2003a).

In the numerical experiments including the salinity effects, the mass of total hydrometeors increases by at most 10%. The liquid water mass increases considerably up to about 20% of the total hydrometeor mass during the eruption, but decreases quickly thereafter. The presence of liquid water during the eruption acceler-

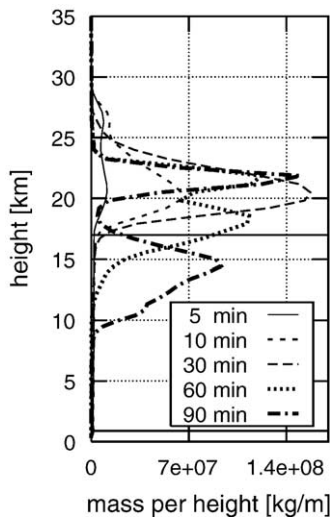


Fig. 10. Vertical distributions of ash particles at $t=5, 10, 30, 60$ and 90 min, shown for the experiment DRY. The plume base level at 750 m and the tropopause at 17 km are indicated by horizontal lines. The scale gives $[\text{kg m}^{-1}]$.

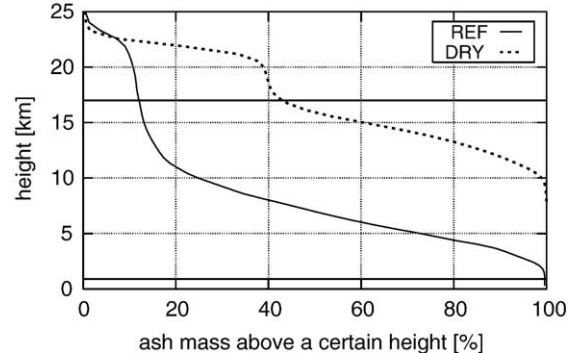


Fig. 11. Mass fractions of erupted ash above a certain height at 90 min simulation time. The plume base level at 750 m and the tropopause at 17 km are indicated by horizontal lines. Shown for the sensitivity experiment DRY without particle aggregation.

erates the aggregation process. However, at the end of the simulations the amount of aggregated particles is not significantly changed when compared to the REF experiment. The sizes and fall velocities of the aggregates generally increase with increasing availability of liquid water in the different experiments. Our simple experiments indicate a strong impact of salinity effects on the volcanic ash aggregation, but more detailed experiments with more comprehensive parameterizations are necessary. These are however outside the scope of this study.

4.4. Modification of the collection efficiency

The sensitivity of ash aggregation to variations of the collection coefficient E is the subject of this section. See also Section 4.7 of Paper I for the description of the representation of the collection efficiency in our approach. We keep the ambient and volcanic conditions as in the REF experiment, but modify the functions f (see Eq. (37) in Paper I) that reflect the availability of hydrometeors at the particle surfaces as given below in Eq. (4) and illustrated in Fig. 12. We employ simple parameterizations, which should cover the range of possible values, while certainly awaiting experimental validation. ϵ is the relevant mass ratio of hydrometeor and ash, see Eq. (38) in Paper I.

$$\begin{aligned}
 f_{\text{REF}}(\epsilon) &= \epsilon \\
 f_{\text{POR1}}(\epsilon) &= 0.5 \cdot \tanh(3\pi(\epsilon - 0.66)) + 0.5 \\
 f_{\text{POR2}}(\epsilon) &= 0.4 \cdot \arctan(2\pi(\epsilon - 0.5)) + 0.5 \\
 f_{\text{LIN1}}(\epsilon) &= 2 \cdot \epsilon \\
 f_{\text{LIN2}} &= 10 \cdot \epsilon
 \end{aligned} \tag{4}$$

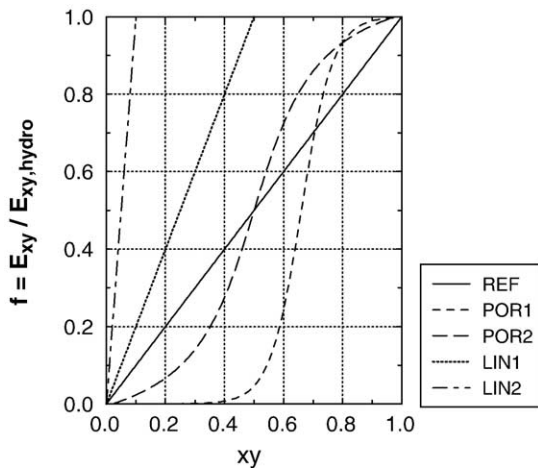


Fig. 12. Functions f given in Eq. (4), which modify the collection efficiencies, versus the hydrometeor fraction given in Eq. (4).

In the study REF, the efficiency is linearly dependent on the hydrometeor fraction of the colliding particles. For hydrometeor fractions larger than 50% the values for pure hydrometeors are applied. In the experiments LIN1 and LIN2 we consider the possibility that less water or ice is sufficient to completely cover the ash core, and we presume hydrometeor fractions of 33% and about 10%, respectively. For an ash particle of 50 μm in radius this is equivalent to a hydrometeor layer of $\Delta r_{\text{REF}}=20.0 \mu\text{m}$, $\Delta r_{\text{LIN1}}=10 \mu\text{m}$, and $\Delta r_{\text{LIN2}}=5 \mu\text{m}$ in the three experiments, respectively. In the experiments POR1 and POR2, the effect of aggregate porosity is examined, and the onset of collection is delayed until higher water fractions are available.

Fig. 13 shows the fraction of particles in the larger size classes during the course of the experiments. Our simulations reveal a high dependency of the fraction of

aggregated particles on the collection efficiency. In the experiment POR2, particle growth is nearly suppressed, because the hydrometeor fraction in the aggregates is in general lower than 10%, see Section 4.1, whereas collection only becomes efficient for hydrometeor fractions larger than 40%, see Fig. 12. The aggregation rate is also slower in the experiment POR1, where the fraction of particles in the larger class is less than half of that in the REF experiment. In the experiments LIN1 and LIN2, the fractions of large ash aggregates are increased, especially in the experiment LIN2, where particle growth is so efficient that millimeter-sized particles are formed. In this latter experiment, aggregates reach the ground about 10 min after the end of the eruption. This removal of large particles from the atmosphere causes the apparent decrease in the fraction of large particles in Fig. 13.

All eruption columns reach the same HNB at ≈ 23 km as in the REF experiment. However, the subsequent fate of ash in the atmosphere is quite different. Fig. 14 shows the mass fractions of erupted ash above a certain height at 90 min simulation time. The amount of small particles suspended at HNB increases with decreasing aggregation efficiency (POR1 > POR2 > REF > LIN1 > LIN2), because fewer small particles are contained in settling aggregates. Increasing collection efficiencies lead at the same time to a decrease in the altitudes of the lower edges of the settling ash layers. In the experiment POR1, ash aggregation is more reduced than in POR2, and consequently the stratospheric cloud in the former contains more than 40% of the erupted ash, whereas the latter contains only about 30%, see Fig. 14. However, the lower boundaries of the fallout zones for these two experiments occur both at a height of about 5 km at the end of our simulation. In POR2, a larger fraction of particles is contained in aggregates,

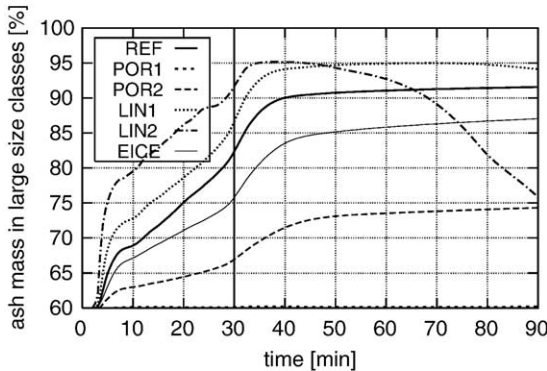


Fig. 13. Mass fractions of particles in the larger size classes during the course of the experiments. The vertical line at 30 min indicates the end of the eruption. Shown for the sensitivity studies regarding the sticking coefficient conditions.

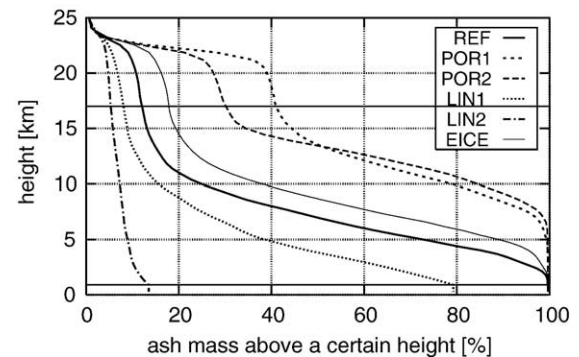


Fig. 14. Mass fractions of erupted ash above a certain height at 90 min simulation time. The plume base level at 750 m and the tropopause at 17 km are indicated by horizontal lines. Shown for the sensitivity experiments about the collection efficiency.

and thus removed from the stratosphere. However, the size of these aggregates, i.e., their fall velocities, is not much larger than in POR1. This result reflects the non-linearity of the ash growth process.

The HNB is lifted during the course of our experiments, as shown in Fig. 15. This post-eruptive rise of the umbrella cloud becomes increasingly evident with increasing separation of larger aggregates from fine ash (and volcanic gases), because sedimentation reduces the density of the remaining umbrella cloud in the stratosphere. Separation develops at an enhanced rate once the volcanic cloud is no longer fed from below, i.e., when gravitational fall-back over the vent occurs. Gravitational separation appears to be strongly enhanced by ash aggregation, and by ice growth on ash.

The impact of the collection efficiency of frozen particles on aggregate growth is explored in an additional sensitivity study. In the experiment REF, we apply the aggregation coefficient for ice particles based on Lin et al. (1983) see Eq. (36) of Paper I. This formulation is applicable to meteorological clouds, but has not been verified for icy ash particles at high altitudes. In an experiment tagged EICE we employ the collection efficiency used in Murakami (1990), which neglects the temperature dependence. The collection efficiencies were modified in all processes, for which two frozen classes interact:

$$E_{\text{ice}} = 0.1. \quad (5)$$

The aggregation coefficient of frozen particles in EICE is larger than that in the REF experiment at all temperatures T below -46°C . The efficiencies given in Eq. (5) hold for pure ice particles. For mixed ice–ash particles, they are modified as in the REF experiment using the function f_{REF} given in Eq. (4). Fig. 13 shows

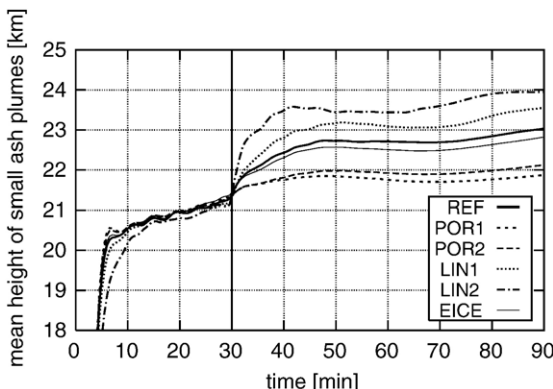


Fig. 15. Height of neutral buoyancy (indicated by the mass weighted mean height of the eruption clouds of the small ash particles) during the course of the simulations for the experiments about the collection efficiency.

that the scavenging of small particles is less efficient in the experiment EICE than in REF. The contribution of large particles to the total ash mass decreases from about 92% to 87%. As a consequence of diminished particle growth, sedimentation is reduced and the particle residence time in the atmosphere is increased, see Figs. 14 and 15.

Because of the current lack of in situ observations, the dependence of the collection efficient E on the availability of hydrometeors at the particle's surface is represented by coarse estimations in this study. In all likelihood, these do not exactly reflect the real dependencies, but should span the range of possible values. We have illustrated here the relevance of having detailed information on the particle morphology, which determines the collection efficiency of the wet and icy aggregation process.

4.5. Electrostatic forces

Within the concept of ATHAM it is impossible at the moment to explicitly simulate the effects of electrostatic forces on ash aggregation, because we do not calculate electric fields. We performed however a series of simplified experiments. We modified the collection efficiencies in the equations for autoconversion, given in Section 4.6.2 of Paper I. In five studies called ELS*, we set the following collection efficiencies: $f_{\text{ELS}1}=0.50$, $f_{\text{ELS}2}=0.25$, $f_{\text{ELS}3}=0.10$, $f_{\text{ELS}4}=0.05$, and $f_{\text{ELS}5}=0.01$, respectively. In order to test the principal influence of electrostatic forces with the highly simplified parameterization in our study, we invoke this process only for small particles in the absence of water, where the process is most significant, see also Sections 3, 4.7, and 5 of Paper I. At locations where hydrometeors occur simultaneously with ash particles, our usual parameterizations for the wet or icy aggregation processes are active, and electrostatic effects are not considered.

Fig. 16 shows the fraction of particles in the larger size classes for the experiments ELS*. The amount of aggregate mass increases with increasing collection efficiency from experiment ELS5 to ELS1. In the experiment ELS1, almost all small particles are scavenged by aggregates. The delay of particle aggregation onset at the beginning of the eruption is shorter than in the REF experiment, because it does not depend on the formation of hydrometeors. The difference in the fractions of large particles is almost entirely determined by the aggregation rate in the high concentration central rising zone, as pointed out in the description in Section 4.1.

At times later than 40 min of simulation, particles do not aggregate to a large degree, because the amount of

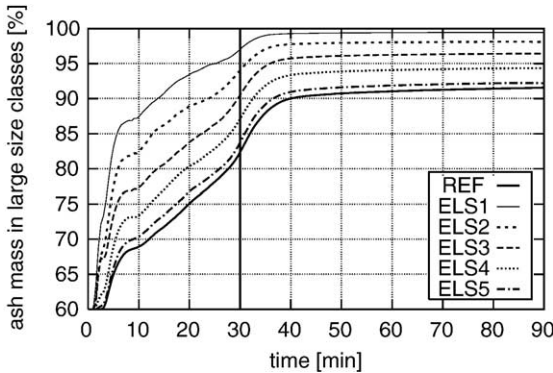


Fig. 16. Mass fractions of particles in the larger size classes during the course of the simulations. The vertical line at 30 min indicates the end of the eruption. Shown for the sensitivity studies ELS*.

dry ash in the small particle classes is limited after the eruption's end and because of the reasons discussed for the REF experiment.

In Fig. 17 the mass fractions of erupted ash above a certain height are plotted at 90 min simulation time. The increased amount of particles contained in aggregates leads to a strong decrease of the amount of small particles suspended in the stratosphere at HNB. In the experiment ELS1 only about 4% of the particles remain in the stratosphere in contrast to about 13% in the REF experiment. Although aggregation efficiencies are quite different for the single experiments, and always higher than in REF, the differences in the lower boundaries of the fallout zones of the column heights are not. The sizes of the aggregates, and thus their fall velocities are only slightly larger than in the REF experiment, and they increase only slightly from experiment ELS5 to ELS1. Although a higher ash fraction is included in aggregates particles, all of them have the same growth probability. Non-linear particle aggregation, which

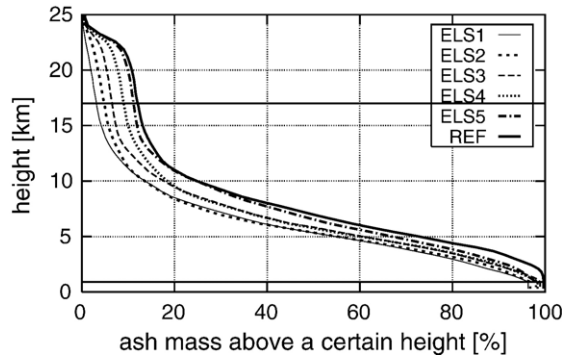


Fig. 17. Mass fractions of erupted ash above a certain height at 90 min simulation time. The plume base level at 750 m and the tropopause at 17 km are indicated by horizontal lines. Shown for the sensitivity experiments ELS*.

would promote the growth of single, larger particles at the cost of others, is not affected. Thus, the size, and fall speed of the aggregates do not change significantly. These results are valid only in the case of invariant electric fields and constant electric properties of aggregating particles as assumed in our experiments. In reality none of these remain constant, and thus, preferential particle growth might occur.

4.6. Size distribution of erupted particles

In this section, we examine the importance of the initial size distribution of erupted particles on the aggregation efficiency. We perform a sensitivity study called ASK under the same conditions as in the REF experiment except for the initial size distribution. Fig. 18 depicts the particle size distribution for the Askja D ash estimated by Woods and Bursik (1991) (WB) as an example for a Plinian eruption, and the gamma functions used in ATHAM to represent this distribution. The initial mean volume radii of ash in the small and the large classes are 10 μm and 100 μm , respectively. The smaller class contributes a mass fraction of 20%. Highly efficient particle growth leads to the formation of millimeter-sized aggregates, as shown in Fig. 19.

The increased particle size in the larger class, and the greater differences in the sizes and fall velocities between the two classes cause significantly enhanced particle growth, because gravitational capture becomes more efficient. Consequently, sedimentation is much more pronounced than in the REF experiment. At the end of the simulation, about 75% of the erupted mass is deposited on the ground. The formation of two ash

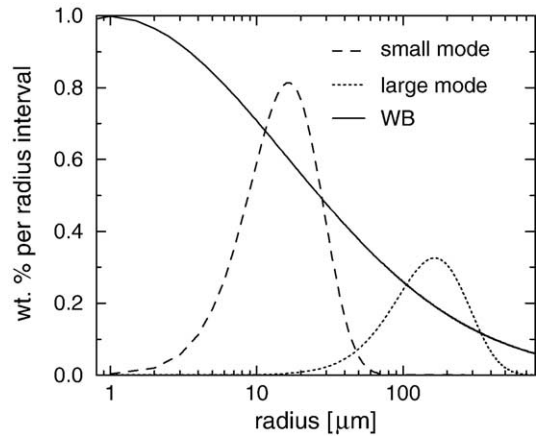


Fig. 18. Particle size distribution of the Askja D ash. The log-normal distribution given by WB (thin solid line) is shown. The two gamma distributions (dashed and dotted lines) represent the particle size distributions of the two ash classes used in ATHAM.

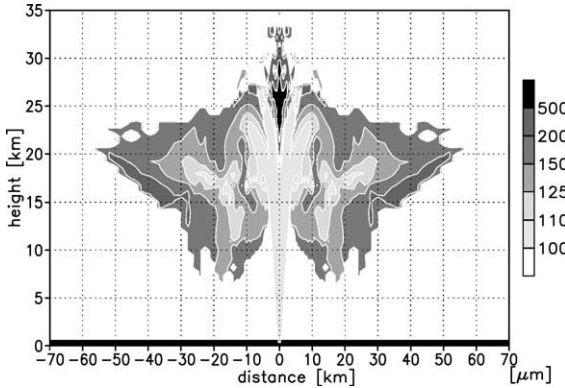


Fig. 19. Mean volume radii of particles in the large frozen mode (x - z distribution) at locations with mass mixing ratios $> 5 \text{ g kg}^{-1}$. Shown at 30 min for the experiment ASK.

zones is less obvious, and the stratospheric mass amounts to about 5%. In addition, the enhanced sedimentation reduces the horizontal expansion of the umbrella cloud by 20 km compared to the REF experiment, after 30 min of eruption. We conclude that an extended knowledge of the initial particle size distribution is crucially needed in order to assess the ash dispersal during explosive volcanic eruptions.

4.7. Ambient conditions

The impact of the environmental conditions on the eruption column's geometry and height was investigated by Glaze and Baloga (1996), Glaze et al. (1997), Woods (1993), Herzog (1998) and Graf et al. (1999). Their studies revealed, that the column height is not only determined by the composition and temperature of the erupting material, or by its vent exit velocity. It also depends on the actual meteorological conditions in the

environment in terms of atmospheric stability and relative humidity. The latent heat release due to phase changes of water contributes a considerable amount to the eruption column's total thermal energy and therefore influences its vertical evolution. This section considers the effect of ambient conditions on ash aggregation efficiency. We use various vertical profiles for temperature and humidity in the background atmosphere shown in Fig. 20, but leave the volcanic forcing the same as in the REF experiment.

The experiments called SAS, SAW, MLS and MLW reflect subarctic summer, subarctic winter, mid-latitude summer and mid-latitude winter conditions, respectively (McClatchey et al., 1972). The subtropical ambient conditions of the REF (see Fig. 2), are modified in the experiments STH and STW, where we increase the temperature and the humidity, respectively, to simulate daily variations. In the experiment TRO we increase both the temperature and the humidity as in the previous two experiments, to resemble tropical conditions. Fig. 21 displays the mass of condensed hydrometeors (liquid water+ice) during the course of the simulations. This hydrometeor mass is in general accordance with the specific humidity in the atmosphere in the experiments, although this is not exactly true for subarctic and mid-latitudinal conditions. Condensed hydrometeors still account only for a few percent of the tephra mass in the Plinian eruption cloud in our experiments, for all ambient conditions, and quite dry aggregates develop. The amount of ice is always about two orders of magnitude greater than that of liquid water. Aggregation of water-coated particles is therefore insignificant, and we do not find an impact of the availability of liquid water on aggregation efficiency.

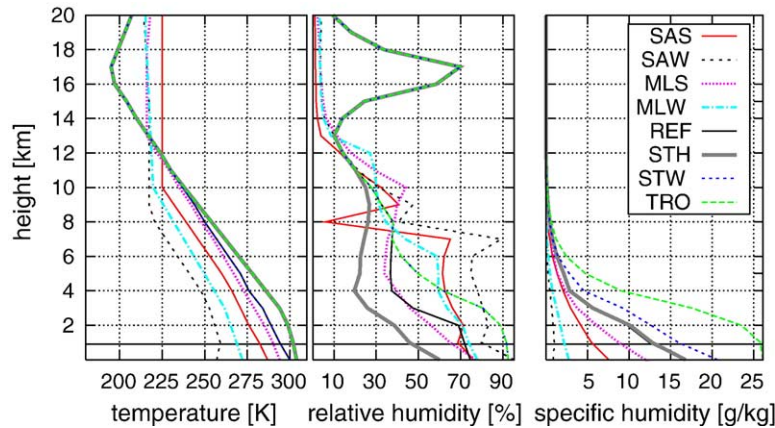


Fig. 20. Atmospheric profiles for temperature and relative, and specific humidity (McClatchey et al., 1972) in the sensitivity experiments regarding the ambient conditions. The plume base level at 750 m is indicated by a horizontal line. The legend is explained in the text.

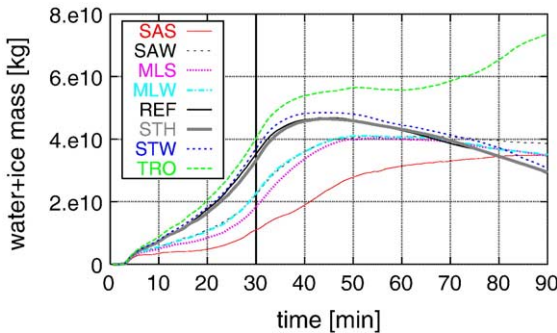


Fig. 21. Mass of total liquid water and ice in the model during the course of the simulations. The vertical line at 30 min indicates the end of the eruption. Shown for the sensitivity studies regarding the ambient conditions.

Fig. 22 shows the fraction of particles in the larger size classes during the course of the simulations. The aggregation efficiency increases in the same sequence as the amount of condensed hydrometeors in the eruption column. It is strongest in the experiment TRO and least effective in the experiment SAS. In contrast to the REF experiment, aggregation persists to some degree in the experiments SAW, MLW, MLS, and especially in SAS, after the collapse of the eruption column at about 40 min simulation time. These experiments show less efficient aggregation during the eruption, hence a higher fraction of small particles is still available. In addition, the stratosphere is warmer under subarctic and mid-latitude conditions, leading to increased collection efficiency of icy particles (see Section 4.4). Under the higher relative humidities between 4 and 8 km (see Fig. 20), sublimation or evaporation of hydrometeors do not occur, and aggregation of the settling particles occurs in the lower troposphere (see also Section 4.1).

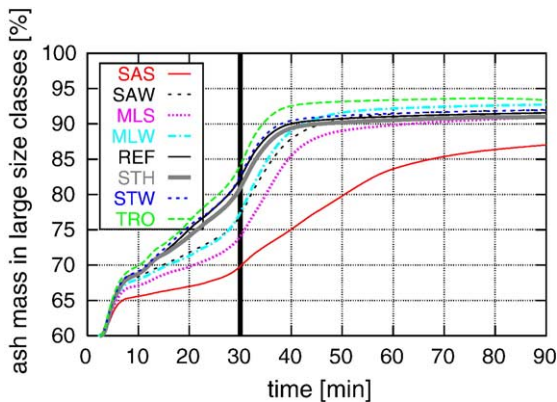


Fig. 22. Mass fractions of particles in the larger size classes during the course of the simulations. The vertical line at 30 min indicates the end of the eruption. Shown for the sensitivity studies regarding the ambient conditions.

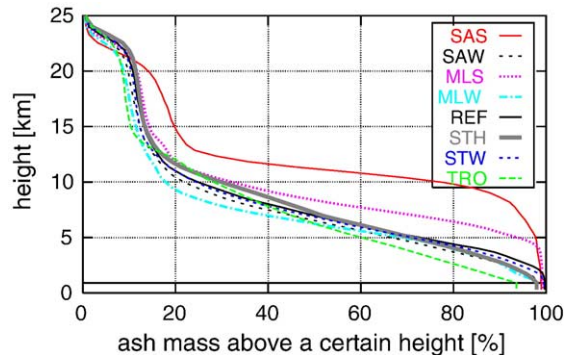


Fig. 23. Mass fractions of erupted ash above a certain height at 90 min simulation time, shown for the sensitivity studies about the ambient conditions. The plume base level at 750 m and the tropopause at 17 km are indicated by horizontal lines.

Fig. 23 shows the mass fractions of erupted ash above a certain height at 90 min simulation time. All curves show two ash layers: a stratospheric cloud of small particles at HNB, and a broader fallout zone of aggregated ash in the troposphere, as described in Sections 4.1 and 4.4. The altitudes of the HNBs increase slightly with increasing specific humidity in the ambient atmosphere, but they are mainly determined by the strong volcanic forcing. The HNBs are situated between 20 and 23 km. Complex mutual dependencies of macro-scale physical and microphysical quantities complicate the interpretation of the results. The stability and humidity of the atmosphere influences dynamics and temperature distribution in the eruption column. At the same time, the aggregation efficiency is influenced, which determines ash fallout and the structure of the flow in the vicinity of the eruption column. It is not possible to assign individual microphysical effects to a single ambient parameter. The effect of the ambient conditions depends on the strength of the eruptions, and becomes less important for stronger eruptions as shown in this study. We did not find a large dependency of the aggregation efficiency on the ambient conditions, except for the experiment SAS. There, the limited availability of condensed hydrometeors reduces aggregation, and thus the separation of the two particle size classes. The HNB is about 2 km lower containing a larger fraction of non aggregated particles, and the fallout zone is about 5 km higher than in REF. During explosive volcanic eruptions with high columns, the aggregation of frozen particles is highly dominant, and the amount of ice determines the amount of aggregation. It is enhanced at warmer stratospheric temperatures, but the temperature dependence of icy ash aggregates is not well established, see Section

4.4, and awaits detailed investigation. In phreatomagmatic eruptions with a much higher availability of water we would assume a much more efficient particle aggregation.

5. Discussion and conclusion

The microphysics of hydrometeors and ash particles in Plinian eruption columns has been studied through numerical experiments with the ATHAM model. The microphysical parameterizations we have employed are introduced and discussed in Paper I of this study. We did not try to simulate a specific event, but chose conditions typical for highly explosive eruptions. Our experiments are meant to test extreme cases in order to understand the sensitivity of the aggregation process to individual parameters.

The aggregation of wet or icy ash due to gravitational capture results in efficient aggregation and increases the particle fall velocities. Two distinct layers of ash develop in our experiments, caused by the separation of the fine fraction (and gases) suspended at HNB from the settling coarser particles. Separation is enhanced through the scavenging of small particles by aggregation from the upper layer, which leads to a density decrease and, thus, to a secondary lifting of the HNB. This is enhanced when the volcanic cloud is no longer fed from below, after the end of the eruption. Thus, particle aggregation influences the height and the residence time of volcanic emissions in the stratosphere.

The total mass of tephra is about two orders of magnitudes greater than that of condensed hydrometeors during Plinian eruptions. Hence, hydrometeor–ash aggregates are rather dry, with ice fractions usually lower than 10% by mass. Most condensed water is frozen to ice in the eruption column, because of the fast rise to regions well above freezing level, and particles occur mainly as fairly dry, icy ash aggregates. A low relative humidity in the lower troposphere as in our simulations causes complete evaporation of hydrometeors. Thus, no traces of them will be observed in the fallout deposits, although water and ice play a significant role during the transport in the column. We only find a weak influence of the atmospheric background conditions on ash microphysics for the strong eruptions in our experiments. Increased specific humidity in the ambient atmosphere leads in general to enhanced ice formation, which in turn slightly enhances aggregation. The ice phase is highly dominant for all tested background atmospheres. Recent satellite observations of volcanic clouds provide strong indirect evidence for the presence of ice, as discussed in Paper I, but ex-

tremely high ice contents are necessary to distinguish its signal from that of silicate particles in the plume. We would expect more significant effects of the ambient conditions on ash aggregation in the case of eruptions containing very large amounts of water or ice in the column, such as phreatomagmatic events, or in the case of less violent eruptions with lower columns and warmer temperatures with higher amount of liquid water.

We assume in this study for the sake of computational efficiency that volcanic particles are always active as condensation nuclei for liquid water and ice. We tested our parameterization in a sensitivity study where we reduced the threshold temperature for ice nucleation by 15°. The results are not modified significantly, because the temperatures are well below this threshold in most regions of the eruption column in our simulations. However, the nucleation capacity of fresh volcanic ash has not yet been characterized by in situ or laboratory observations.

Gravitational capture becomes more efficient for greater differences in the sizes and fall velocities between the two size classes, thus causing significantly enhanced particle growth. Eruptions with identical mass eruption rates but contrasting particle size distributions can result in completely different ash–hydrometeor distributions in the atmosphere. More detailed information on the erupted particle size distribution, which is very sparse to date, would be desirable. The availability of hydrometeors at the particles' surfaces, determines the collection efficiency and thus particle growth. Wet ash particles have a higher sticking capacity than icy ones. Aggregation is thus most efficient within the column where limited regions of liquid water exist and where particle concentrations are very high. Our simplified experiments show an influence of the temperature also on the aggregation efficiency of ice-covered particles. Warmer stratospheric temperatures favor icy-ash aggregation. First studies considering the salinity effects show an increase in the amount of total water and ice, and of the liquid water fraction, thus increasing aggregation efficiency. The existence of a quasi-liquid layer at the particles' surface (Faraday, 1859) might act in the same direction, but the characteristics of such a layer remain highly uncertain (Pruppacher and Klett, 1997). Our results show also that the particle morphology is a key parameter for ash aggregation, because it determines the amount of hydrometeors available as adhesive for aggregate formation. These results indicate the need for research on surface properties and the porosity of volcanic particles, especially at low temperatures. Many uncertainties exist about the stability of ash aggregates. The parameterization in this study does

not include breakup processes. Large aggregates may be destroyed due to hydrodynamic instabilities during settling or due to collision with other particles, as in the breakup of large raindrops. Water evaporation in the relatively dry lower troposphere leads to drying of settling particles, and this may enhance the breakup rate of aggregates.

We investigated the potential importance of electrostatic forces on ash aggregation. Since the ATHAM model does not provide any information on electric fields during the eruption, we varied the collection efficiencies for small, dry ash, for which these forces are most significant, in a series of sensitivity experiments. The experiments show that electrostatics strongly increase the aggregation of small particles, and that the degree of aggregation is highly sensitive to the choice of the electrostatic collection efficiency. In our study, all particles have the same growth probability, non-linear particle aggregation, which would promote the growth of single, larger particles at the cost of others, is not affected by electrostatic aggregation. The sizes, fall speeds, and thus the sedimentation pattern, do not change significantly. This result is valid for invariable electric fields and constant electric properties of the aggregating particles. We believe that in reality none of these will remain constant, and therefore, more efficient preferential particle growth might occur. Our study provides however an initial assessment of the microphysical effects of the electrostatic aggregation mechanism.

Very little data exist for particle properties within eruption columns. In this exploratory study we have therefore used simple parameterizations for ash aggregation which should reflect the range of possible values, see also the discussion in Section 5 of Paper I about the limitations of our parameterization. We have identified important processes controlling the particle scavenging efficiency and the parameters, which determine these processes. Our assumptions and results will need to be rigorously tested against laboratory and in situ data in order to reduce the uncertainty about particle microphysics within Plinian eruption columns.

Acknowledgments

C. Textor, H.-F. Graf and M. Herzog thank the Volkswagen Foundation for supporting the development of the ATHAM model. C. Textor thanks M. Schulz and the Laboratoire des Sciences du Climat et de l'Environnement, France, for the opportunity to complete this study. G.G.J. Ernst thanks the Max-Planck-Institut für Meteorologie for welcoming him in

the Hamburg group and for generous financial support. He also thanks the Fondation Belge de la Vocation (Golden Clover Award), the Nuffield Foundation (NAL award), and the Belgian NSF (FWO-Vlaanderen) for current support at U. Ghent. We would also like to thank the two anonymous reviewers, especially for indicating the importance of electrostatic and hygroscopic effects.

References

- Carey, S., Sigurdsson, H., 1982. Influence from particle aggregation on deposition of distal tephra from the May 18, 1980, eruption of Mount St. Helens volcano. *Journal of Geophysical Research* 87 (B8), 7061–7072.
- Faraday, M., 1859. On regulation, and on observation of force. *Philosophical Magazine* 17, 162–169.
- Glaze, L.S., Baloga, S.M., 1996. Sensitivity of buoyant plume heights to ambient atmospheric conditions: implications for volcanic eruption columns. *Journal of Geophysical Research* 101 (D1), 1529–1540.
- Glaze, L.S., Baloga, S.M., Wilson, L., 1997. Transport of atmospheric water vapor by volcanic eruption columns. *Journal of Geophysical Research* 102 (D5), 6099–6108.
- Graf, H.-F., Herzog, M., Oberhuber, J.M., Textor, C., 1999. The effect of environmental conditions on volcanic plume rise. *Journal of Geophysical Research* 104, 24309–24320.
- Herzog, M., Graf, H.-F., Textor, C., Oberhuber, J.M., 1998. The effect of phase changes of water on the development of volcanic plumes. *Journal of Volcanology and Geothermal Research* 87, 55–74.
- Herzog, M., Oberhuber, J.M., Graf, H., 2003. A prognostic turbulence scheme for the non-hydrostatic plume model ATHAM. *Journal of the Atmospheric Sciences* 60, 2783–2796.
- Holasek, R.E., Woods, A.W., Self, S., 1996. Experiments on gas–ash separation processes in volcanic umbrella plumes. *Journal of Volcanology and Geothermal Research* 70 (3–4), 169–181.
- Lane, S.J., Gilbert, J.S., 1992. Electric potential gradient changes during explosive activity at Sakurajima volcano, Japan. *Bulletin of Volcanology* 54 (7), 590–594.
- Lin, Y., Farley, R.D., Orville, H.D., 1983. Bulk parametrization of the snow field in a cloud model. *Journal of Climate and Applied Meteorology* 22, 1065–1092.
- Mackinnon, I.D.R., Gooding, J.L., McKay, D.S., Clanton, U.S., 1984. The El Chichón stratospheric cloud: solid particulates and settling rates. *Journal of Volcanology and Geothermal Research* 23, 125–146.
- McClatchey, R.A., Fenn, R.W., Selby, J.E.A., Volz, F.E., Garing, J.S., 1972. Optical Properties of the Atmosphere, (3rd ed). Environmental Research Papers, vol. 411.
- Miura, T., Koyaguchi, T., Tanaka, Y., 1996. Atmospheric electric potential gradient measurements of ash clouds generated by pyroclastic flows at Unzen volcano, Japan. *Geophysical Research Letters* 23 (14), 1789–1792.
- Murakami, M., 1990. Numerical modeling of dynamical and microphysical evolution of an isolated convective cloud—The 19 July 1981 CCOPE Cloud. *Journal of the Meteorological Society of Japan* 68 (2).
- Oberhuber, J.M., Herzog, M., Graf, H.-F., Schwanke, K., 1998. Volcanic plume simulation on large scales. *Journal of Volcanology and Geothermal Research* 87, 29–53.

- Pruppacher, H.R., Klett, J.D., 1997. Microphysics of Clouds and Precipitation, 2nd Edition. Kluwer Academic Publishers.
- Schneider, D.J., Rose, W.I., Coke, L.R., Bluth, G.J.S., 1999. Early evolution of a stratospheric volcanic eruption cloud as observed with TOMS and AVHRR. *Journal of Geophysical Research* 104 (D4), 4037–4050.
- Smith, B.D., Zielinski, R.A., Rose, W.I., Huebert, B.J., 1982. Water-soluble material on aerosols collected within volcanic eruption clouds. *Journal of Geophysical Research* 87 (C7), 4963–4972.
- Sparks, R.S.J., Bursik, M.I., Carey, S.N., Gilbert, J.S., Glaze, L., Sigurdsson, H., Woods, A.W., 1997. *Volcanic Plumes*. Wiley and Sons, New York.
- Textor, C., Graf, H.-F., Herzog, M., Oberhuber, J.M., 2003a. Injection of gases into the stratosphere by explosive volcanic eruptions. *Journal of Geophysical Research* 108 (D19). doi:[10.1029/2002JD002987](https://doi.org/10.1029/2002JD002987).
- Textor, C., Sachs, P.M., Graf, H.-F., Hansteen, T.H., 2003b. The 12,900 yr BP Laacher See eruption: estimation of volatile yields and simulation of their fate in the plume. In: Oppenheimer, C., Pyle, D., Barclay, J. (Eds.), *Volcanic Degassing*, Geological Society, London, Special Publications, vol. 213, pp. 307–328.
- Textor, C., Graf, H.-F., Herzog, M., Oberhuber, J.M., Rose, W.I., Ernst, G.G.J., 1993. Volcanic particle aggregation in explosive eruption columns. Part I: Parameterization of the microphysics of hydrometeors and ash. *Journal of Volcanology and Geothermal Research* 150, 359–377.
- Trentmann, J., Andreae, M.O., Graf, H.-F., Hobbs, P.V., Ottmar, R.D., Trautmann, T., 2002. Simulation of a biomass-burning plume: comparison of model results with observations. *Journal of Geophysical Research*. doi:[10.1029/2001JD000410](https://doi.org/10.1029/2001JD000410).
- Trentmann, J., Andreae, M.O., Graf, H.-F., 2003. Chemical processes in a young biomass-burning plume. *Journal of Geophysical Research* 108 (D22). doi:[10.1029/2003JD003732](https://doi.org/10.1029/2003JD003732).
- Woods, A.W., 1993. Moist convection and the injection of volcanic ash into the atmosphere. *Journal of Geophysical Research* 98, 17627–17636.
- Woods, A.W., Bursik, M.I., 1991. Particle fallout, thermal disequilibrium and volcanic plumes. *Bulletin of Volcanology* 53, 559–570.